Production and Characterization of Cellulose Acetate-Graphene Oxide Composite Membrane as Proton Exchange Membrane Fuel Cell

Riki Haryanto, Shafira Ayuningtyas, Pratiwi Pudjiastuti, and Siti Wafiroh*

Department of Chemistry, Faculty of Science and Technology, Universitas Airlangga, Campus C, Mulyorejo, Surabaya 60115, Indonesia

** Corresponding author:*

tel: +62-85645217900
email: sitiwafiroh@fst.unair.ac.id

Received: November 4, 2025
Accepted: January 3, 2026

DOI: 10.22146/ijc.112830

Abstract: *The global energy crisis caused by dependence on fossil fuels has accelerated the search for renewable and sustainable energy sources, such as the proton exchange membrane fuel cell (PEMFC). This study aimed to develop cellulose acetate–graphene oxide (CA–GO) composite membranes with different GO concentrations (0–2%) to enhance proton-exchange performance. Cellulose acetate was characterized by molecular weight determination and Fourier-transform infrared spectroscopy (FTIR), while graphene oxide was synthesized via the Hummers method and analyzed using X-ray diffraction (XRD), FTIR, and electrochemical impedance spectroscopy (EIS). The CA–GO membranes were fabricated by the phase-inversion method and evaluated for mechanical strength, swelling ratio, ion-exchange capacity (IEC), proton conductivity, and methanol permeability. The membrane containing 2% GO showed the best performance, with a Young's modulus of 1.344 MPa, swelling ratio of 7%, IEC of 0.147 meq/g, methanol permeability of 1.2×10^{-3} kg/m²·s, and proton conductivity of 1.59×10^{-4} S/cm. FTIR analysis indicated hydrogen bond formation between CA and GO, while SEM revealed a heterogeneous surface morphology. These results demonstrate that incorporating 2% GO improves the mechanical strength and proton conductivity of CA membranes without significantly increasing methanol permeability, indicating potential for PEMFC applications.*

Keywords: *fuel cell; PEMFC; cellulose acetate; graphene oxide*

Accepted

■ INTRODUCTION

Global energy consumption has continued to increase substantially, while more than 80% of the world's energy demand remains dependent on fossil fuels such as petroleum, natural gas, and coal [1]. This increasing energy demand, driven by population growth and socio-economic development, has raised serious concerns regarding energy security and environmental sustainability due to the continued reliance on conventional energy sources [2]. Consequently, the growing disparity between rising energy demand and the limited availability of natural resources has intensified global efforts to develop sustainable, efficient, and environmentally benign alternative energy technologies, including wind energy, biofuels, and fuel cells [3].

A fuel cell is an electrochemical device that directly converts the chemical energy of fuels, such as hydrogen or methanol, into electrical energy without combustion [4]. In a fuel cell, the fuel is oxidized at the anode while oxygen is reduced at the cathode, and the electron transfer between these reactions generates an electrical current [5]. This technology exhibits high energy conversion efficiency, produces no harmful emissions, and can continuously generate electrical power as long as the fuel supply is maintained [6-7]. Among various types of fuel cells, the proton exchange membrane fuel cell (PEMFC) is considered the most promising due to its low operating temperature, high efficiency, short start-up time, and excellent chemical stability [8-9].

The main component of a PEMFC is the membrane electrode assembly (MEA), which consists of an anode, a cathode, and an electrolyte membrane [10]. Among various types of membranes, Nafion®, a perfluorosulfonic acid (PFSA)-based polymer, is widely

utilized because it exhibits a high proton conductivity of 0.0983 S/cm. However, Nafion® exhibits several drawbacks, including high production costs, decreased conductivity above 100°C, and high methanol permeability of approximately 1.37×10^{-6} cm^2/s [11-12]. These limitations have motivated the exploration of alternative membrane materials that are more cost-effective, environmentally friendly, and more thermally and mechanically stable [2].

Natural polymers, particularly cellulose acetate (CA), have emerged as promising candidates for membrane materials due to their biodegradability, non-toxicity, hydrophilicity, and ease of modification [13-14]. However, pure CA exhibits several drawbacks, including low proton conductivity (< 10^{-6} S/cm), high water uptake (71.6%), relatively low mechanical strength (9.7 MPa), and limited thermal and chemical stability [15-16]. Various modification strategies have been employed to enhance these properties. For example, Eldin et al. [17] reported that sulfonated cellulose acetate exhibited excellent thermal stability up to 375.72 °C, high mechanical strength (49.25 N), and low methanol permeability (1.729×10^{-17} cm^2/s). Najafi et al. [18] also found that CA membranes exhibited good thermal stability up to 224 °C, while Samaniego et al. [19] reported an ion exchange capacity (IEC) of 2.15 mmol/g. Moreover, Laksono and Aji [16] observed that the proton conductivity of pure CA (1.54×10^{-6} S/cm) could be enhanced to 2.95×10^{-4} S/cm by incorporating LiCl at a 65/35 ratio. Another effective strategy to further improve the proton conductivity and mechanical performance of CA membranes involves adding inorganic fillers, such as GO. GO is rich in oxygen-bearing groups and has a broad surface area, enabling strong hydrogen bonding with the polymer framework and thereby enhancing the mechanical integrity and the chemical and electrochemical performance of CA membranes [20-21].

GO is a chemically altered derivative of graphene produced through the exfoliation of graphite, with an approximate C/O ratio of 2.1. It has a two-dimensional, single-layer configuration consisting of sp^2- and sp^3-hybridized carbon atoms, functionalized with oxygenated moieties, including –OH, –COOH, and epoxy groups [22]. GO is typically prepared by the conventional or modified Hummers method, in which natural flake graphite (NFG) is oxidized in the presence of oxidizing agents such as potassium permanganate and sodium nitrate. Despite the generation of harmful gaseous byproducts, including NO_2 and N_2O_4, this route remains one of the most effective and extensively utilized techniques for large-scale GO synthesis [23]. GO exhibits several advantageous properties, including a large surface area (736.6 m^2/g), hydrophilicity, high proton conductivity, and low gas permeability (2.1914 Barrer) [24]. The presence of acidic functional groups and extensive hydrogen-bond networks facilitates proton transport, leading to ionic conductivity approaching 10^{-2} S/cm [21]. Furthermore, its high-water uptake capacity (approximately 30% after 3 h) enhances proton conduction under hydrated conditions [25]. In PEMFC applications, GO has attracted significant attention as a proton-conductive filler and reinforcing agent due to its hydrophilicity, thermal stability, and ability to form π–π interactions with polymer matrices [22,26]. Therefore, incorporating GO into CA matrices is expected to yield composite membranes with higher proton conductivity, reduced methanol permeability, and enhanced mechanical and thermal stability, suitable for PEMFC applications.

In this study, CA–GO composite membranes were prepared with varying GO concentrations (0, 0.5, 1, 1.5, and 2%). GO was produced via an improved Hummers procedure and subsequently analyzed by XRD and FTIR. The cellulose acetate–GO composite membranes were prepared via a phase-separation technique and evaluated for their mechanical (swelling ratio, tensile strength, and Young's modulus) and electrochemical characteristics (proton conductivity, ion-exchange capacity, and methanol permeability). The most suitable membrane for PEMFC applications was further examined by FTIR and SEM to verify its structural and surface morphology features.

■ EXPERIMENTAL SECTION

Materials

All chemicals and reagents used in this study were of analytical or reagent grade and were used without

Accepted

further purification unless otherwise specified. CA (Mn ~50,000), acetone (CH_3COCH_3; analytical grade, ≥ 97%), graphite powder (< 20 μm, 99%), sodium nitrate ($NaNO_3$; 99%), hydrogen peroxide (H_2O_2; 30%, reagent grade), potassium chloride (KCl; ≥ 99%), and methanol (CH_3OH; 99.8%) were obtained from Sigma-Aldrich (USA). Sodium hydroxide pellets (NaOH; 99%), sulfuric acid (H_2SO_4; 98%, reagent grade), potassium permanganate ($KMnO_4$; 99%), and hydrochloric acid (HCl; 37%) were purchased from Merck (Germany). Distilled water and phenolphthalein indicator were used as received. Distilled water and phenolphthalein indicator were used as received.

Instrumentation

Characterization of materials was conducted utilizing an X-ray diffractometer (XRD, Shimadzu XRD-7000, Japan), a Fourier Transform Infrared spectrometer (FTIR, Perkin Elmer Paragon 1000PC, USA), and a scanning electron microscope (SEM, JEOL JSM-8360LA, Japan). Membrane tensile properties were determined using a universal mechanical testing system (Shimadzu AG-1S 50 kN Autograph, Japan), and viscosity was measured via a Brookfield viscometer (Brookfield, USA). Electrochemical impedance spectroscopy (EIS) data were obtained through an automatic LCR meter (Fluke and Philips PM 6303A, The T&M Alliance, Netherlands). The IEC was evaluated through acid–base titration, while methanol permeability was analyzed using a dead-end filtration assembly.

Procedure

Synthesis and characterization of membrane raw materials

GO was synthesized through a modified Hummers method. In this method, graphite powder (5 g, < 20 μm, 99%, Sigma-Aldrich) was mixed with $NaNO_3$ (2.5 g, 99%) and concentrated H_2SO_4 (115 mL, 98%, Merck) under continuous stirring in an ice bath maintained at 0–10 °C. $KMnO_4$ (15 g, 99%) was then slowly added while keeping the reaction temperature below 10 °C, and the mixture was stirred for an additional 2 h. The suspension was subsequently heated to 35 ± 3 °C for 30 min until a brownish paste was obtained. Afterwards, 230 mL of deionized water was carefully added dropwise, followed by dilution with 700 mL of water and the addition of 10 mL of H_2O_2 solution (30%). The mixture was left to stand for 24 h. The resulting product was washed several times with HCl (37%) and deionized water, filtered, and dried to yield the GO powder [27].

The crystalline properties of GO were examined by XRD using Cu Kα radiation (λ = 1.5406 Å) operated at 40 kV, with a 2θ range of 5° to 90°. A 1.5 g sample of CA (Mn ~ 50,000, Sigma-Aldrich) was dissolved in 500 mL of acetone. Its intrinsic viscosity (η) was determined and subsequently correlated with the viscosity-average molecular weight (Mv) using the Mark–Houwink equation [28].

Functional group analysis of CA and GO was conducted using an FTIR in the range of 4000–500 cm^{-1}, with samples prepared as KBr pellets (1:100 w/w). The crystalline structure of GO was examined by XRD using Cu Kα radiation (λ = 1.5406 Å) at 40 kV and a 2θ range of 5–90°. Proton conductivity was measured via electrochemical impedance spectroscopy (Automatic RCL Meter, Fluke & Philips PM 6303A, Netherlands) in the frequency range of 10^5–0.01 Hz with an amplitude of 0.01 mV, using GO pellets prepared under 10 bar pressure and impregnated with 0.5 M H_2SO_4 electrolyte [29].

Preparation of CA–GO composite membrane

The CA–GO composite was fabricated via a phase-inversion immersion method, following the procedure reported by Madih et al. [30] with minor modifications. A total of 10 g of CA was dissolved in 45 mL of acetone under continuous magnetic stirring for 2 h to form a homogeneous polymer solution. Subsequently, GO was incorporated into the mixture in varying concentrations (0–2 wt.% relative to the CA weight; 0, 0.5, 1.0, 1.5, and 2.0%) and mixed for an additional hour to achieve uniform dispersion [31]. The resulting CA–GO blend was sonicated for 30 min in an ultrasonic bath and then allowed to stand for 24 h to remove entrapped air bubbles. The overall fabrication process is schematically illustrated in Fig. 1.

The casting process began by preparing a clean glass plate, which was covered with tape along its edges to

Accepted

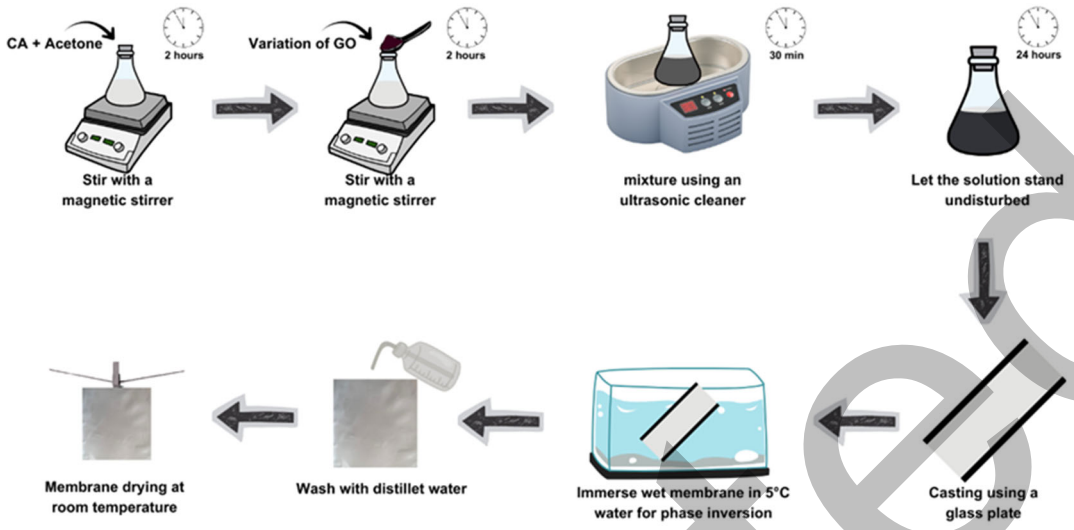

Fig 1. Preparation of CA–GO composite membrane

define the desired membrane thickness. The previously degassed polymer mixture was poured and evenly spread across the plate using a stainless-steel applicator. The freshly cast film was then immersed in a cold distilled water bath (5 °C) to induce phase inversion and enable membrane formation. Once detachment from the substrate occurred, the membrane was repeatedly washed with running water to remove any solvent residues and dried naturally at room temperature [32]. The produced CA–GO composite membranes were preserved in a NaN_3 solution to prevent microbial growth [31].

Characterization of CA–GO composite membranes

Mechanical tests. The membrane's mechanical characteristics were analyzed employing a universal testing apparatus (Autograph). The membrane was shaped into a dumbbell, and its thickness was measured with a micrometer screw gauge. The sample was clamped at both ends and stretched at a rate of 5 mm·min^{-1} at room temperature until failure. The stress (σ), strain (ε), and Young's modulus were calculated using Eq. (1–3), respectively;

$$\sigma = \frac{F}{A} \quad (1)$$

$$\varepsilon = \frac{\Delta L}{l_0} \quad (2)$$

$$E = \frac{\sigma}{\varepsilon} \quad (3)$$

where σ is the tensile stress (N·m^{-2}), ε is the strain, F is the applied force (N), A is the cross-sectional area of the membrane (m^2), ΔL is the elongation at break (m), and l_0 is the initial gauge length (m).

The swelling degree was determined by immersing pre-dried membrane samples (5 × 5 cm^2) in distilled water for 45 min at room temperature. The swollen membranes were surface-dried and reweighed. The swelling degree was calculated using Eq. (4);

$$\text{Swelling} = \frac{W_{wet} - W_{dry}}{W_{dry}} \quad (4)$$

where swelling is the membrane swelling ratio (%), W_{wet} indicates the mass of the hydrated membrane (kg), and W_{dry} indicates the mass of the dry membrane (kg).

Performance tests. Performance characterization included IEC and methanol permeability. The IEC was determined by acid–base titration after the membranes were immersed in 2 M KCl for 12 h. Subsequently, a 10 mL portion of the resulting supernatant was titrated with 0.01 M NaOH solution using phenolphthalein as an indicator, and the IEC value was obtained according to Eq. (5);

$$\text{IEC} = \frac{N_{NaOH}}{W_{dry}} \times V_{NaOH} \quad (5)$$

where IEC is the ion exchange capacity (meq/g), N_{NaOH} is the concentration of NaOH (M), V_{NaOH} is the volume of NaOH (mL), and W_{dry} is the dry sample weight (g).

Accepted

Methanol permeability was evaluated through a dead-end filtration system. Circular membranes (6 cm^2) were exposed to 5 M methanol at 1 atm. The permeate volume was recorded over time, and permeability was calculated using Eq. (6);

$$J = \frac{V \times \rho}{A \times t} \quad (6)$$

where J denotes the permeate flux ($kg/m^2 \cdot s$), *V* represents the volume of liquid collected in the receptor cell (L), ρ is the density of the permeating solution (kg/L), A refers to the effective surface area of the membrane (m^2), and *t* corresponds to the total filtration duration (s).

Characterization of the optimal CA–GO composite membrane

The CA–GO composite membrane with optimal properties was selected based on high tensile strength, low strain, high Young's modulus, low swelling degree, and relatively high IEC. The selected membrane was further characterized to evaluate its structural, morphological, and electrochemical properties.

Functional group analysis was performed by FTIR–ATR over the wavenumber range of 4000–500 cm^{-1} at a resolution of 1 cm^{-1}. Morphological characterization was conducted using a SEM following cryo-fracturing in liquid nitrogen and subsequent gold–palladium coating, operated at 15 kV with magnifications ranging from 1000× to 15,000×. Proton conductivity was determined via EIS over a frequency range of 10^5–0.01 Hz with an amplitude of 0.01 mV at ambient temperature. The membrane sample (2 cm diameter) was placed in a three-electrode test cell and moistened with 0.5 M H_2SO_4 electrolyte. Proton conductivity (κ, $S \cdot cm^{-1}$) was calculated using Eq. (7);

$$k = \frac{L}{R_b \times A} \quad (7)$$

where k is the proton conductivity (S/cm), L is the membrane thickness (cm), R_b is the bulk resistance (Ω), A is the membrane area (cm^2), and d is the membrane diameter (cm).

■ RESULTS AND DISCUSSION

Synthesis and Characterization of GO

GO was successfully synthesized using a modified Hummers method through the oxidation of graphite with $KMnO_4$ under a strongly acidic condition (H_2SO_4) [32]. The oxidation treatment incorporated oxygen-bearing functional groups within the graphite layers, thereby enhancing their hydrophilic properties. The color change from dark black to brown indicated the formation of GO.

The XRD pattern of GO (Fig. 2(a)) exhibited several sharp diffraction peaks at 2θ = 10.70°, 20.65°, 26.43°, 29.08°, 31.13°, and 42.37°. The characteristic peak at 10.70° corresponds to the (001) crystal plane, indicating an increased interlayer spacing due to the insertion of oxygen functionalities [33-34]. These findings are consistent with previous studies. Siburian et al. [33] reported a characteristic GO peak at 2θ = 11.60°, while Al-Gaashani et al. [34] observed a similar diffraction peak at approximately 10.90°, both associated

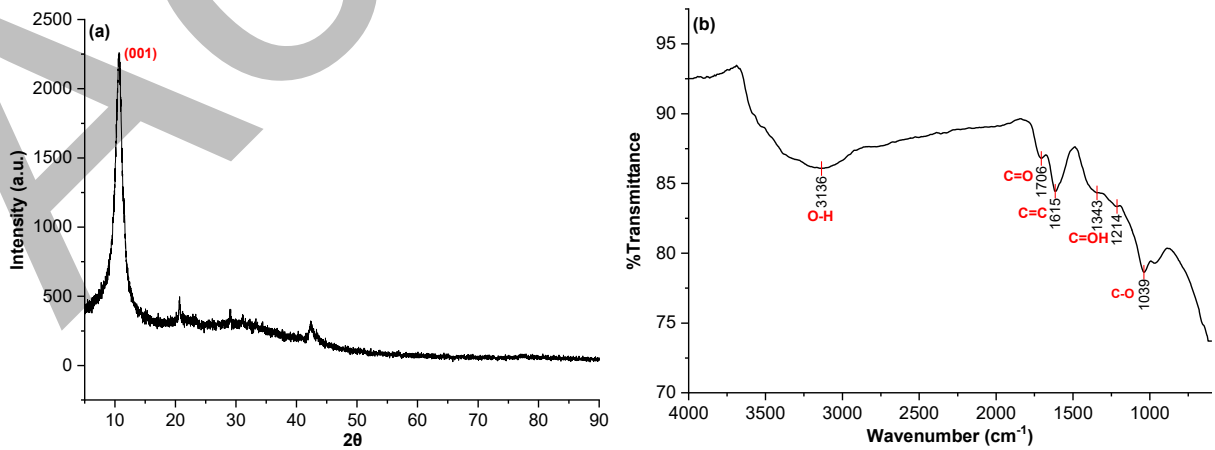

Fig 2. (a) XRD pattern and (b) FTIR spectrum of GO

Accepted

with expanded *d*-spacing due to oxidation. Fatmawati et al. [35] also observed sharp GO peaks at 2θ = 10.487° and 42.327°, further supporting the formation of oxygen-functionalized layered structures. The sharpness of these peaks indicates partial crystallinity in GO, indicating that graphite has been successfully converted into GO, with larger interlayer distances arising from the presence of oxygen-bearing groups. These groups not only increase the spacing between carbon layers but also enhance hydrophilicity by forming polar functional domains (Hung et al.) [36].

The FTIR spectrum (Fig. 2(b)) showed prominent absorption bands attributed to O–H stretching (3136 cm^{-1}), C=O stretching (1706 cm^{-1}), aromatic C=C stretching (1615 cm^{-1}), O–H bending (1343 cm^{-1}), and C–O–C (1214 cm^{-1}) and C–O stretching (1039 cm^{-1}). The presence of these bands confirms the incorporation of hydroxyl, carbonyl, aromatic, and epoxy groups, typical of GO [37]. Proton conductivity refers to the ability of a material to transport protons through its structure [38]. This property plays a crucial role in proton transfer processes and directly influences the overall performance of PEMFC. A higher proton conductivity generally corresponds to lower internal resistance and improved electrochemical efficiency [39]. In this study, proton conductivity analysis using electrochemical impeandce spectroscopy (EIS), as shown in Fig. 3, revealed that GO exhibited a conductivity of 0.255 S/cm, which is significantly higher than that of the reference Nafion membrane (0.086 S/cm). This enhanced conductivity is attributed to the presence of abunandt hydrophilic functional groups and well-developed proton transport pathways within the GO layers [40].

Characterization of CA

The average molecular weight of the CA polymer was determined using a Brookfield viscometer. This analysis aimed to obtain the intrinsic viscosity and average molecular weight of the CA polymer [41]. The intrinsic viscosity data obtained from the measurements were subsequently used to determine the average molecular weight (Mv) using the Mark–Houwink equation [28].

Measurements were conducted with a Brookfield NDJ series viscometer equipped with spindle number 1.

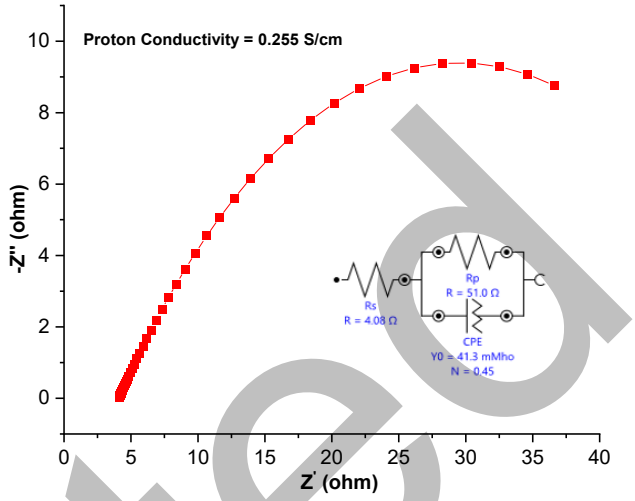

Fig 3. Nyquist plot and fitted circuit of GO proton conductivity

The test was repeated three times at room temperature to ensure consistent results and minimize experimental errors. The polymer solution was prepared at a concentration of 0.10% to facilitate measurement. The results showed an η of 1 mPa s and an average molecular weight ($\overline{Mv}$) of 4.1×10^4 g/mol, which is comparable to the standard CA molecular weight of approximately 5.0×10^4 g/mol. The slightly lower intrinsic viscosity and molecular weight observed in this study are likely due to minor chain degradation of CA during dissolution or stirring. Stirring can influence polymer dissolution, altering the molecular weight distribution and the resulting viscosity, particularly in polymers with high molar mass [42].

FTIR analysis was performed to characterize the functional groups present in the CA polymer. The resulting FTIR spectrum of CA is presented in Fig. 4. The absorption band at 3484 cm^{-1} corresponds to O–H stretching, 1735 cm^{-1} to C=O stretching, 1368 cm^{-1} to –CH_2– deformation, 1218 cm^{-1} to C–O–C asymmetric stretching, and 1030 cm^{-1} to C–O stretching. These results are consistent with the standard CA spectra [43], confirming the presence of hydroxyl, carbonyl, and ether functional groups in the polymer. The FTIR spectrum indicates that the chemical structure of the synthesized CA is in agreement with standard cellulose acetate, supporting its suitability for further membrane fabrication.

Accepted

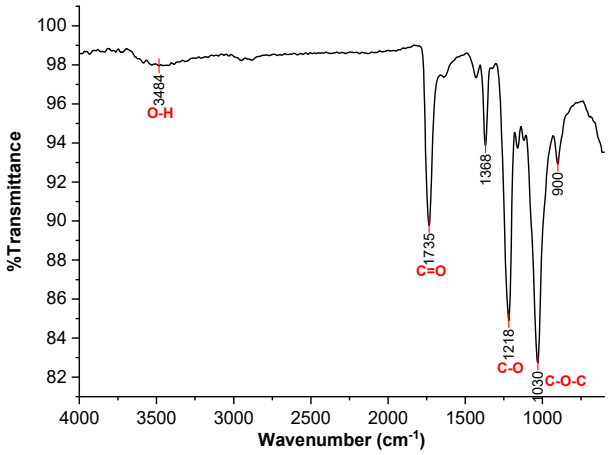

Fig 4. FTIR spectrum of the CA polymer sample

Fabrication of CA–GO Composite Membranes

The CA–GO composite membranes were successfully fabricated via the phase-inversion immersion technique with GO concentrations of 0, 0.5, 1.0, 1.5, and 2.0%. The obtained membranes exhibited uniform morphology, good flexibility, and were free from visible defects. Phase inversion is a fabrication approach in which a polymer solution is transformed into a solid matrix through a controlled demixing process. The process starts with liquid–liquid phase separation, resulting in two immiscible liquid phases. The polymer-enriched phase then solidifies, forming a compact network that serves as the membrane's main framework.

Mechanical tests

The tensile properties of the CA–GO composite membranes were evaluated using an Autograph tensile tester to determine their mechanical strength, strain, and Young's modulus. Membrane thicknesses were measured using a micrometer, and dumbbell-shaped specimens were tested at a crosshead speed of 10 mm/min at room temperature. The measured thicknesses for membranes containing 0, 0.5, 1.0, 1.5, and 2.0% GO were 0.01, 0.03, 0.02, 0.02, and 0.03 mm, respectively. The optimum membrane thickness for fuel cell applications ranges from 30 to 100 μm (0.03–0.10 mm) [44]. Achieving an optimal membrane thickness is essential to balance ion conductivity, fuel transport, and mechanical stability, thereby ensuring maximum performance and efficiency [45]. In this study, membranes with a thickness of 0.03 mm (at GO loadings of 0.5 and 2.0%) fall within the optimal range for fuel cell applications, whereas the thinner membranes (0.01–0.02 mm) fall below the recommended thickness range.

The tensile stress of the pristine CA membrane (0% GO) was 17.36 MPa, whereas the CA–GO composite membranes exhibited slightly lower stress values due to GO incorporation. The membrane with 2.0% GO exhibited the highest stress among the composites at 12.24×10^6 N/m^2, indicating that GO enhanced membrane strength and network density [46]. The lowest stress was observed at 0.5% GO, likely due to less homogeneous polymer–GO interactions.

Strain values decreased with increasing GO content, reflecting reduced elasticity as the composite structure became denser. The highest strain was observed for the pristine CA membrane (27.11), while the lowest strain was found for the 2.0% GO membrane (9.11) [47]. This trend indicates that the addition of GO restricts polymer chain mobility, enhancing stiffness but reducing extensibility.

The Young's modulus also increased with GO concentration, from 0.641 MPa for the pristine CA membrane to 1.344 MPa for the 2.0% GO membrane, confirming that GO reinforcement improves mechanical rigidity [48]. Overall, the CA–GO composite membrane with 2.0% GO achieved an optimal balance of mechanical properties, demonstrating enhanced strength and modulus while maintaining acceptable strain values.

Swelling refers to the volumetric expansion of a material upon direct contact with gases, vapors, or liquids [49]. This characteristic serves as an indicator of membrane hydrophilicity and its capacity to absorb water. The swelling process does not induce chemical bond formation within polymer chains but rather disrupts intermolecular interactions. A denser membrane structure limits water diffusion into the material [50]. In organic solvents, swelling is critical for determining the membrane's performance in proton exchange, as volumetric expansion increases membrane thickness and enhances diffusivity of components due to the separation of polymer chains [51]. The swelling degree of CA–GO composite membranes with varying GO concentrations (0, 0.5, 1.0, 1.5, and 2.0%) is presented in Table 1.

Accepted

Table 1. Results of mechanical testing for CA–GO composite membranes at different GO concentrations

Concentration of GO (%)	Stress (MPa)	Strain	Young modulus (MPa)	Swelling (%)
0	17.369 ± 2.498	27.108 ± 5.253	0.641 ± 0.03	17.13 ± 3.36
1	1.535 ± 1.212	9.111 ± 2.727	0.168 ± 0.08	10.24 ± 3.131
2	8.593 ± 2.487	12.614 ± 3.334	0.681 ± 0.02	10.56 ± 1.685
3	10.350 ± 2.920	12.389 ± 1.919	0.835 ± 0.107	11.91 ± 3.215
4	12.240 ± 1.936	9.110 ± 1.282	1.344 ± 0.02	7.37 ± 0.771

The results indicate that the membrane with the highest GO content (2.0%) exhibited the lowest swelling degree of 7%. This trend suggests that increasing GO concentration reduces free volume in the membrane matrix, thereby limiting water molecule penetration [52]. Excessive swelling can compromise membrane mechanical stability, reducing operational lifespan and suitability for application [53]. For comparison, the swelling value of the CA–GO membrane with 2.0% GO is significantly lower than that of Nafion, which exhibits a swelling degree of 28.7% [54].

Performance tests

IEC represents a material's capability to reversibly transfer ions between the membrane and the surrounding medium [55]. This characteristic plays a vital role in assessing ion transport performance within membranes, as it indicates the quantity of active functional groups responsible for ion exchange [56]. Cation-exchange membranes possess negatively charged functional groups that enable cation migration, whereas anion-exchange membranes contain positively charged sites that promote anion movement [57]. The IEC value is influenced by the abundance of functional groups embedded in the membrane structure [58]. The IEC of CA–GO composite membranes was evaluated using an acid–base titration method, which measures the material's ion-exchange capacity [59]. The IEC results are presented in Fig. 5.

As shown in Fig. 5, the membrane without GO exhibited an IEC of 0.104 meq/g. Increasing the GO content in the CA–GO membranes increased the negative charge density by allowing ester functional groups in cellulose acetate to interact with GO's oxygen-containing groups, thereby improving the ion exchange capacity [60]. The highest IEC was observed for the membrane containing 2.0% GO, with a value of 0.147 meq/g. Despite

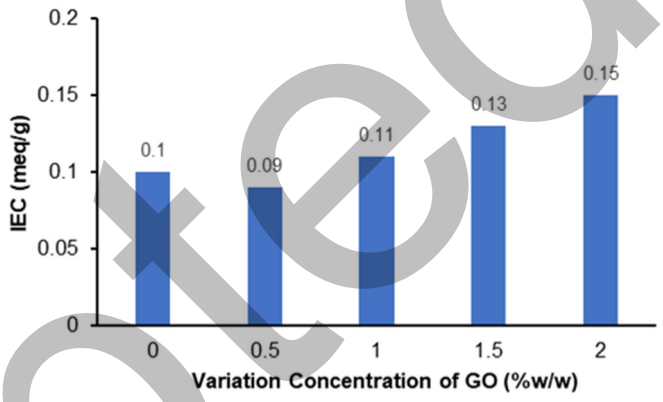

Fig 5. IEC values of CA–GO composite membranes with varying GO concentrations (%)

this increase, the IEC of CA–GO membranes remains lower than that of Nafion, which has an IEC of 0.9 meq/g (9×10^{-4} eq/g) [61]. Higher IEC values indicate a more effective ion exchange, which is essential for optimal membrane performance.

Methanol permeability is an important parameter for determining the membrane's ability to resist methanol transfer from the anode to the cathode [62]. This assessment evaluates how effectively the membrane can hinder methanol movement through its matrix. Permeability testing was carried out utilizing a glass diffusion apparatus consisting of two symmetrical chambers [63]. The results are presented in Fig. 6.

As illustrated in Fig. 6, the methanol permeability exhibited by the unmodified CA membrane (0% GO) was 1.6×10^{-3} kg/m^2 s. The addition of GO to the CA framework decreased methanol permeability. The minimum permeability value was obtained for the CA–GO membrane containing 2% GO, maintaining a value of 1.2×10^{-3} kg/m^2 s. This decline is ascribed to enhanced interfacial interactions and membrane rigidity, which reduce the void fraction on the membrane surface, consequently restricting methanol diffusion [64]. A more

Accepted

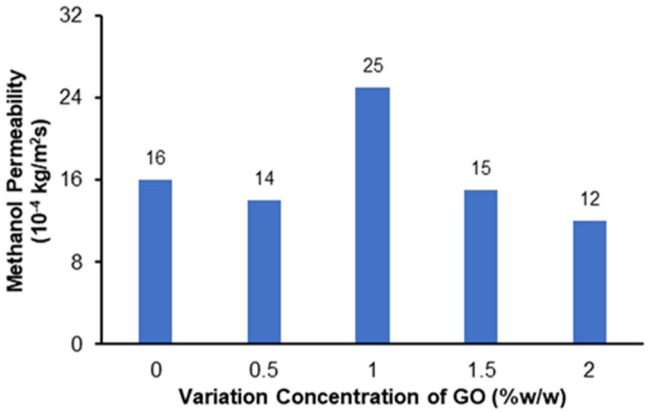

Fig 6. Methanol permeability of CA–GO composite membranes with varying GO concentrations (%)

robust membrane structure generally corresponds to reduced methanol permeability [63]. Although improvement was observed, the methanol permeability of the CA–GO (2% GO) membrane is still higher than that of Nafion, which exhibits a permeability of 3.611×10^{-4} kg/m^2 s. Reducing methanol permeability is advantageous for fuel cell membrane applications, as it helps suppress crossover and improve overall system efficiency.

Characterization of the Optimal CA–GO Composite Membrane

FTIR characterization was performed to determine the functional groups present in the membrane samples. The FTIR spectra of CA polymer, GO, and the CA–GO composite membranes are presented in Fig. 7. The CA polymer exhibits characteristic absorption peaks at 3441 cm^{-1} (O–H stretching), 1731 cm^{-1} (C=O stretching), 1370 cm^{-1} (–CH_2– deformation), 1218 cm^{-1} (C–O–C asymmetric stretching), and 1028 cm^{-1} (C–O stretching). The broadening of the O–H stretching peak at 3441 cm^{-1} indicates the formation of hydrogen bonding between CA and GO [65]. The additional absorption peak at 1640 cm^{-1} in the CA–GO composite corresponds to C=C stretching, confirming the incorporation of graphene oxide [37]. A proposed interaction mechanism between CA and GO in the composite membrane is illustrated in Fig. 8.

SEM provides high-resolution imaging and comprehensive insights into the microscopic characteristics of materials, including dimensions, morphology, structural

Fig 7. FTIR spectra of CA, GO, and CA–GO composite membranes

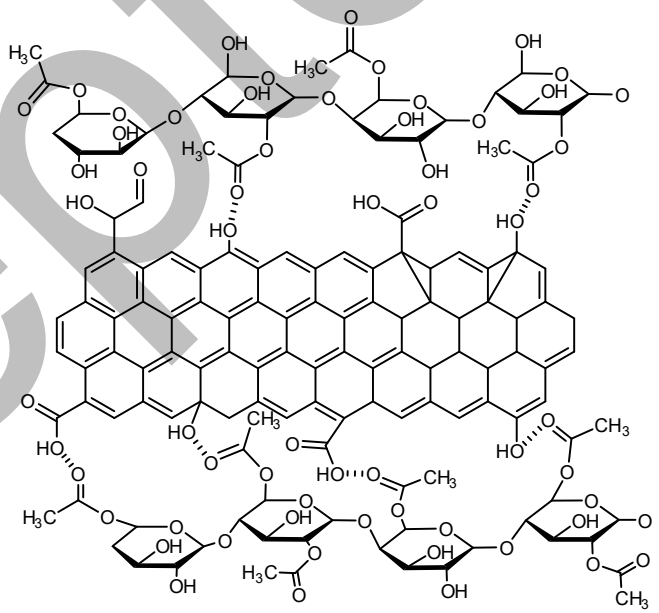

Fig 8. Proposed interaction mechanism between cellulose acetate and graphene oxide in CA–GO composite membranes

arrangement, crystallinity, and various physicochemical properties [66]. SEM is extensively utilized to investigate the surface morphology of porous membranes [67]. In this research, SEM was used to examine the surface and cross-sectional structures of the CA–GO composite membranes, enabling analysis of pore distribution, surface topology, and macrovoid formation.

The composite membranes were initially frozen using liquid nitrogen and then carefully sectioned with tweezers. Before SEM analysis, the specimens were

Accepted

coated with a thin gold–palladium film. SEM observations were performed at an accelerating voltage of 15 kV, with magnifications of 1,000, 5,000, 10,000, and 15,000×. The surface structure of the CA–GO composite membrane containing 2.0% GO is presented in Fig. 9(a–d).

The SEM images (Fig. 9(a–d)) reveal a rough membrane surface with randomly distributed GO particles and pores appearing at several sites. The irregular distribution and surface roughness are attributed to insufficient homogeneity during the stirring of the CA–GO dope solution and the presence of trapped air bubbles [68-69]. Additional contributing factors include contamination from dust or debris remaining on the glass casting plate during membrane fabrication [70]. The formation of surface pores is a consequence of the phase inversion process during immersion in the coagulation bath. The solvent diffuses out while the non-solvent (water) diffuses into the membrane, creating voids and a porous structure [71]. Increasing the GO concentration in the composite membrane results in a denser, more rigid structure that restricts solvent diffusion and produces smaller pore sizes [72].

Proton conductivity is a key parameter reflecting a material's ability to transport protons, which directly influences fuel cell performance [38]. Higher proton conductivity values generally indicate improved membrane performance [73]. The CA–GO composite membranes were evaluated in a three-electrode split test cell using 0.5 M H_2SO_4 as the electrolyte. EIS was performed over a frequency range of 10^5–0.01 Hz with an AC signal amplitude of 0.01 mV [74]. The Nyquist plot and the equivalent circuit model for the CA–GO membrane are illustrated in Fig. 10.

The fitting analysis of the CA–GO composite membrane indicated a relatively high standard deviation (χ^2 = 0.10113), which may be attributed to suboptimal circuit fitting and the membrane's fragile nature during testing [75]. The measured proton conductivity of the CA–GO composite membrane was 0.0159×10^{-2} S/cm, which is significantly lower than that of the commercial Nafion standard (0.086 S/cm). The reduced proton conductivity of the CA–GO membrane is likely due to its denser structure and its relatively low content of ion-conducting functional groups compared to Nafion, which

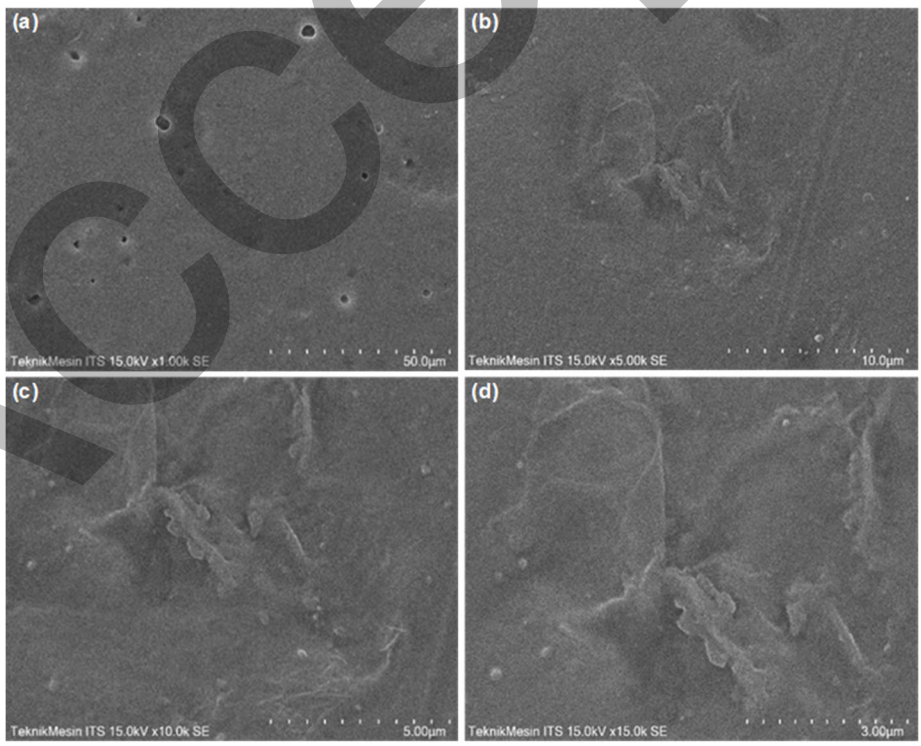

Fig 9. SEM images of the CA–GO composite membrane (2.0% GO) surface at magnifications of (a) 1,000×, (b) 5,000×, (c) 10,000×, and (d) 15,000×

Accepted

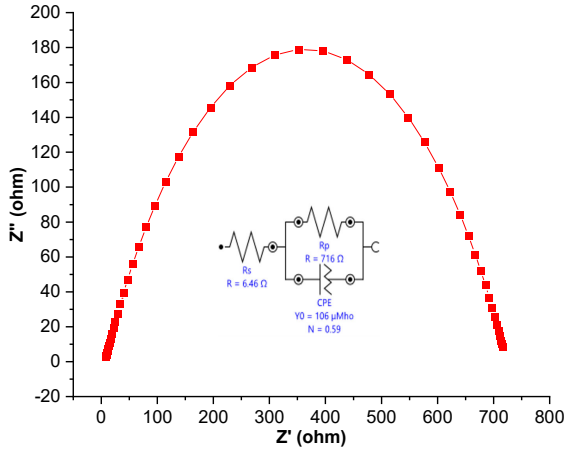

Fig 10. Nyquist plot and equivalent circuit fitting of the CA–GO composite membrane

limit proton transport pathways within the composite.

CONCLUSION

The incorporation of GO markedly enhanced the structural, transport, and mechanical properties of CA membranes. Among the investigated compositions, the CA–GO membrane containing 2% GO exhibited the most balanced performance, characterized by increased ion-exchange capacity, reduced methanol permeability and swelling, and improved mechanical strength. These improvements are attributed to strong interfacial interactions between CA and GO, which promote a denser membrane structure and hinder methanol crossover. Although proton conductivity remains lower than that of Nafion, the overall performance, combined with material sustainability and cost-effectiveness, makes the CA–GO membrane a promising alternative for PEMFC applications. Future work should focus on nanoscale dispersion and functionalization of GO to further enhance proton transport properties.

ACKNOWLEDGMENTS

The authors sincerely thank the Department of Chemistry, Faculty of Science and Technology, Universitas Airlangga, for providing access to laboratory facilities and analytical instruments, as well as for the valuable support that enabled this research.

CONFLICT OF INTEREST

There are no conflicts to declare.

AUTHOR CONTRIBUTIONS

Riki Haryanto: funding, investigation, validation, data curation, visualization, writing –original draft; Shafira Ayuningtyas: investigation, validation; Pratiwi Pudjiastuti: methodology, investigation, writing – review and editing; Siti Wafiroh: investigation, validation, methodology, writing - review and editing. All authors agreed to the final version of the manuscript.

REFERENCES

[1] International Energy Agency (IEA), 2021, *World Energy Outlook 2021*, IEA Publications, Paris, France.

[2] Owusu, P.A., and Asumadu-Sarkodie, S., 2016, A review of renewable energy sources, sustainability issues and climate change mitigation, *Cogent Eng.*, 3 (1), 1167990.

[3] Niakolas, D.K., Daletou, M., Neophytides, S.G., and Vayenas, C.G., 2016, Fuel cells are a commercially viable alternative for the production of "clean" energy, *Ambio*, 45 (1), 32–37.

[4] Wang, C., Wang, S., Peng, L., Zhang, J., Shao, Z., Huang, J., Sun, C., Ouyang, M., and He, X., 2016, Recent progress on the key materials and components for proton exchange fuel cells in vehicle applications, *Energies*, 9 (8), 603.

[5] Derbeli, M., Barambones, O., Silaa, M.Y., and Napole, C., 2020, Real-time implementation of a new MPPT control method for a DC-DC boost converter used in a PEM fuel cell power system, *Actuator*, 9 (4), 105.

[6] Olabi, A.G., Wilberforce, T., and Abdelkareem, M.A., 2021, Fuel cell application in the automotive industry and future perspective, *Energy*, 214, 118955.

[7] Ahmed, K., Farrok, O., Rahman, M.M., Ali, M.S., Haque, M.M., and Azad, A.K., 2020, Proton exchange membrane hydrogen fuel cell as the grid connected power generator, *Energies*, 13 (24), 6679.

Accepted

[8] Yang, Y., Ma, T., Du, B., Lin, W., and Yao, N., 2021, Investigation on the operating conditions of proton exchange membrane fuel cell based on constant voltage cold start mode, *Energies*, 14 (3), 660.

[9] Wang, S., and Jiang, S.P., 2017, Prospects of fuel cell technologies, *Natl. Sci. Rev.*, 4 (2), 163–166.

[10] Baroutaji, A., Carton, J., Sajjia, M., and Olabi, A.G., 2016, "Materials in PEM Fuel Cells" in *Reference Module in Materials Science and Materials Engineering*, Elsevier, Amsterdam, Netherlands, 1–11.

[11] Zakaria, Z., Kamarudin, S.K., Timmiati, S.N., and Masdar, M.S., 2019, New composite membrane poly(vinyl alcohol)/graphene oxide for direct ethanol–proton exchange membrane fuel cell, *J. Appl. Polym. Sci.*, 136 (2), 46928.

[12] Karimi, M.B., Mohammadi, F., and Hooshyari, K., 2019, Recent approaches to improve Nafion performance for fuel cell applications: A review, *Int. J. Hydrogen Energy*, 44 (54), 28919–28938.

[13] Roberson, C., 2019, *Cellulose Acetate: Properties, Uses, and Preparation*, Nova Science Publishers, Inc., New York, US.

[14] Kusworo, T.D., Soetrisnanto, D., Widayat, W., Budiyono, B., and Utomo, D.P., 2018, Study of polymeric membranes potential for eugenol purification from crude clove leaf oil, *ASEAN J. Chem. Eng.*, 18 (2), 81–92.

[15] Etemadi, H., Yegani, R., Seyfollahi, M., and Rabiee, M., 2018, Synthesis, characterization, and anti-fouling properties of cellulose acetate/polyethylene glycol-grafted nanodiamond nanocomposite membranes for humic acid removal from contaminated water, *Iran. Polym. J.*, 27 (6), 381–393.

[16] Laksono, E.W., and Aji, D., 2016, Conductivity of cellulose acetate membranes from panand duri leaves (*Panandus tectorius*) for Li-ion battery, *MATEC Web Conf.*, 64, 04001.

[17] Mohy Eldin, M.S., Abd Elmageed, M.H., Omer, A.M., Tamer, T.M., Yossuf, M.E., and Khalifa, R.E., 2016, Novel proton exchange membranes based on sulfonated cellulose acetate for fuel cell applications: preparation and characterization, *Int. J. Electrochem. Sci.*, 11 (12), 10150–10171.

[18] Najafi, M., Sadeghi, M., Bolverdi, A., Pourafshari Chenar, M., and Pakizeh, M., 2017, Gas permeation properties of cellulose acetate/silica nanocomposite membrane, *Adv. Polym. Technol.*, 37, 2043–2052.

[19] Samaniego, A.J., Arabelo, A.K., Sarker, M., Mojica, F., Madrid, J., Chuang, P.Y.A., Ocon, J., and Espiritu, R., 2020, Fabrication of cellulose acetate-based radiation grafted anion exchange membranes for fuel cell application, *J. Appl. Polym. Sci.*, 138 (10), 49947.

[20] Yadav, R., Subhash, A., Chemmenchery, N., and Kandasubramanian, B., 2018, Graphene and graphene oxide for fuel cell technology, *Ind. Eng. Chem. Res.*, 57 (29), 9333–9350.

[21] Shi, B., Wu, H., Shen, J., Cao, L., He, X., Ma, Y., Li, Y., Li, J., Xu, M., Qiu, M., Geng, H., Yang, P., and Jiang, Z., 2019, Control of edge/in-plane interactions toward robust, highly proton conductive graphene oxide membranes, *ACS Nano*, 13 (9), 10366–10375.

[22] Chee, W.K., Lim, H.N., Huang, N.M., and Harrison, I., 2015, Nanocomposites of graphene/polymers: A review, *RSC Adv.*, 5 (83), 68014–68051.

[23] Alam, S.N., Sharma, N., and Kumar, L., 2017, Synthesis of graphene oxide (GO) by modified Hummers method and its thermal reduction to obtain reduced graphene oxide (rGO), *Graphene*, 6 (1), 1–18.

[24] Choudhary, O.P., dan Choudhary, P., 2017, Scanning Electron Microscope: Advantages and Disadvantages in Imaging Components, *Int. J. Curr. Microbiol. Appl. Sci.*, 6 (5), 1877 1882

[25] Chowdury, M.S.K., Park, S.B., and Park, Y.I., 2020, Graphene oxide-hydrogen membrane fuel cell, *Int. J. Precis. Eng. Manuf.–Green Technol.*, 7 (3), 669–681.

[26] Ami Faiz, M.S., Che Azurahanim, C., Yazid, Y., Suriani, A.B., and Siti Nurul Ain, M.J., 2020, Preparation and characterization of graphene oxide from tea waste and its photocatalytic application of TiO_2/graphene nanocomposite, *Mater. Res. Express*, 7 (1), 015613.

Accepted

[27] Supriyanto, G., Rukman, N.K., Nisa, A.K., Jannatin, M., Piere, B., Abdullah, A., Fahmi, M.Z., and Kusuma, H.S., 2018, Graphene oxide from Indonesian biomass: Synthesis and characterization, *BioResources*, 13 (3), 4832–4840.

[28] Benahmed, A., Azzaoui, K., El Idrissi, A., Belkheir, H., Said Hassane, S.O., Touzani, R., and Rhazi, L., 2022, Cellulose acetate-*g*-polycaprolactone copolymerization using diisocyanate intermediates and the effect of polymer chain length on surface, thermal, and antibacterial properties, *Molecules*, 27 (4), 1408

[29] Shekhar, S., Sharma, R., Sharma, S., Sharma, B., Sarkar, A., and Jain, P., 2020, An exploration of electrocatalytic analysis and antibacterial efficacy of electrically conductive poly (*D*-glucosamine)/graphene oxide bionanohybrid, *Carbohydr. Polym.*, 240, 116242.

[30] Madih, K., El-Shazly, A.H., Elkady, M.F., Aziz, A.N., Youssef, M.E., and Khalifa, R.E., 2022, A facile synthesis of cellulose acetate reinforced graphene oxide nanosheets as proton exchange membranes for fuel cell applications, *J. Saudi Chem. Soc.*, 26 (2), 101435.

[31] Shen, B., and Pu, H., 2020, Poly(ether sulfone)s with pendent imidazolium for anion exchange membranes via click chemistry, *Polymer*, 207, 122944.

[32] Hou, Y., Lv, S., Liu, L., and Liu, X., 2020, High-quality preparation of graphene oxide via the Hummers' method: Understanding the roles of the intercalator, oxidant, and graphite particle size, *Ceram. Int.*, 46 (2), 2392–2402.

[33] Siburian, R., Sihotang, H., Raja, S.L., Supeno, M., and Simanjuntak, C., 2018, New route to synthesize of graphene nano sheets, *Orient. J. Chem.*, 34 (1), 182–187.

[34] Al-Gaashani, R., Najjar, A., Zakaria, Y., Mansour, S., and Atieh, M.A., 2019, XPS and structural studies of high quality graphene oxide and reduced graphene oxide prepared by different chemical oxidation methods, *Ceram. Int.*, 45 (11), 14439–14448.

[35] Fatmawati, D.A., Triyono, T., Trisunaryanti, W., Oktaviano, H.S., and Chasanah, U., 2021, The influence of permanganate enhancement to graphite on chemical structure and properties of graphene oxide material generated by improved Tour method, *Indones. J. Chem.*, 21 (5), 1086–1096.

[36] Hung, W.S., Lin, T.J., Chiao, Y.H., Sengupta, A., Hsiao, Y.C., Wickramasinghe, S.R., Hu, C.C., Lee, K.R., and Lai, J.Y., 2018, Graphene-induced tuning of the d-spacing of graphene oxide composite nanofiltration membranes for frictionless capillary action-induced enhancement of water permeability, *J. Mater. Chem. A*, 6 (40), 19445–19454.

[37] Ghaseminezhad, S.M., Barikani, M., and Salehirad, M., 2019, Development of graphene oxide–cellulose acetate nanocomposite reverse osmosis membrane for seawater desalination, *Composites, Part B*, 161, 320–327.

[38] Ryu, S., Lee, B., Kim, J.H., Pak, C., and Moon, S.H., 2021, High-temperature operation of PEMFC using pore-filling PTFE/Nafion composite membrane treated with electric field, *Int. J. Energy Res.*, 45 (13), 19136–19146

[39] Colpan, C.O., Nalbant, Y., and Ercelik, M., 2018, Fundamentals of fuel cell technologies, *Compr. Energy Syst.*, 4, 1107–1130.

[40] Mishra, S., and Hansora, D., 2018, "Types of Graphene-Related Advanced Nanomaterials" in *Graphene Nanomaterials: Fabrication, Properties and Applications*, Pan Stanford Publishing, Singapore, 3–5.

[41] Pérez, E., Alviso, D., Manrique, E., and Artana, G., 2022, Estimation of the rheological curve of HPAM solutions from measurements using the Brookfield viscometer, *J. Pet. Sci. Eng.*, 216, 110793.

[42] Valois, P., Verneuil, E., Lequeux, F., and Talini, L., 2016, Understanding the role of molar mass and stirring in polymer dissolution, *Soft Matter*, 12 (39), 8143–8154.

[43] Sudiarti, T., Wahyuningrum, D., Bundjali, B., and Made Arcana, I., 2017, Mechanical strength and ionic conductivity of polymer electrolyte

Accepted

membranes prepared from cellulose acetate–lithium perchlorate, *IOP Conf. Ser.: Mater. Sci. Eng.*, 223 (1), 012052.

[44] Junoh, H., Jaafar, J., Md Nordin, N.A.H., Ismail, A.F., Othman, M.H.D., Rahman, M.A., Aziz, F., and Yusof, N., 2020, Performance of polymer electrolyte membrane for direct methanol fuel cell application: Perspective on morphological structure, *Membranes*, 10 (3), 34.

[45] Choi, H.J., Choi, H.J., Kim, J., Choi, H., Chu, C., La, I., Ahn, C.Y., Shim, H., Kim, O.H., and Cho, Y.H., 2025, Comparison on the impact of membrane thickness on the performance of proton exchange membrane-based electrochemical devices, *Int. J. Hydrogen Energy*, 119, 161–172.

[46] Jiang, C., Zhang, L., Li, P., Sun, H., Hou, Y., and Niu, Q.J., 2020, Ultrathin film composite membranes fabricated by novel *in situ* free interfacial polymerization for desalination, *ACS Appl. Mater. Interfaces*, 12 (22), 25304–25315.

[47] Salama, A., Mohamed, A., Aboamera, N.M., Osman, T., and Khattab, A., 2018, Characterization and mechanical properties of cellulose acetate/carbon nanotube composite nanofibers, *Adv. Polym. Technol.*, 37, 2446–2451.

[48] Longo, M., De Santo, M.P., Esposito, E., Fuoco, A., Monteleone, M., Giorno, L., and Jansen, J.C., 2018, Force spectroscopy determination of Young's modulus in mixed matrix membranes, *Polymer*, 156, 22–29.

[49] Agarwal, A., Gupta, S., and Sharma, R., 2016, "Hypoosmotic Swelling Test (HOS)" in *Andrological Evaluation of Male Infertility*, Springer International Publishing, Cham, Switzerland, 93–96.

[50] Asghar, M.R., Zhang, W., Su, H., Zhang, J., Liu, H., Xing, L., Yan, X., and Xu, Q., 2025, A review of proton exchange membranes modified with inorganic nanomaterials for fuel cells, *Energy Adv.*, 4, 185–223.

[51] Kárászová, M., Bourassi, M., and Gaálová, J., 2020, Membrane removal of emerging contaminants from water: Which kind of membranes should we use?, *Membranes*, 10 (11), 305.

[52] Rynkowska, E., Fatyeyeva, K., Marais, S., Kujawa, J., and Kujawski, W., 2019, Chemically and thermally crosslinked PVA-based membranes: Effect on swelling and transport behavior, *Polymers*, 11 (11), 1799.

[53] Sun, X., Shi, S., Fu, Y., Chen, J., Lin, Q., Hu, J., Li, C., Li, J., and Chen, X., 2020, Embrittlement induced fracture behavior and mechanisms of perfluorosulfonic-acid membranes after chemical degradation, *J. Power Sources*, 453, 22789.

[54] Xu, G., Wu, Z., Wei, Z., Zhang, W., Wu, J., Li, Y., Li, J., Qu, K., and Cai, W., 2020, Non-destructive fabrication of Nafion/silica composite membrane via swelling-filling modification strategy for high temperature and low humidity PEM fuel cell, *Renewable Energy*, 153, 935–939.

[55] Yasukawa, M., Suzuki, T., and Higa, M., 2018, "Chapter 1 – Salinity Gradient Processes: Thermodynamics, Applications, and Future Prospects" in *Membrane-Based Salinity Gradient Processes for Water Treatment and Power Generation*, Eds. Sarp, S., and Hilal, N., Elsevier, Amsterdam, Netherlands, 3–56.

[56] Kumar, P., Bharti, R.P., Kumar, V., and Kundu, P.P., 2018, "Chapter 4 – Polymer Electrolyte Membranes for Microbial Fuel Cells: Part A. Nafion-Based Membranes" in *Progress and Recent Trends in Microbial Fuel Cells*, Elsevier, Amsterdam, Netherlands, 47–72.

[57] Sharma, M., Mondal, P., Sontakke, A.D., Chakraborty, A., and Purkait, M.K., 2021, High performance graphene-oxide doped cellulose acetate-based ion exchange membrane for environmental remediation applications, *Int. J. Environ. Anal. Chem.,* 1–22.

[58] Krishna, B.A., Lindhoud, S., and de Vos, W.M., 2021, Hot-pressed polyelectrolyte complexes as novel alkaline stable monovalent-ion selective anion exchange membranes, *J. Colloid Interface Sci.*, 593, 11–20.

[59] Mondragón, R., Juliá, J.E., Cabedo, L., and Navarrete, N., 2018, On the relationship between the specific heat enhancement of salt-based

Accepted

nanofluids and the ionic exchange capacity of nanoparticles, *Sci. Rep.*, 8 (1), 7532.

[60] Zeng, L., Zhao, T.S., Wei, L., Jiang, H.R., and Wu, M.C., 2019, Anion exchange membranes for aqueous acid-based redox flow batteries: Current status and challenges, *Appl. Energy*, 233-234, 622–643.

[61] Mazzapioda, L., Panero, S., and Navarra, M.A., 2019, Polymer electrolyte membranes based on Nafion and a superacidic inorganic additive for fuel cell applications, *Polymers*, 11 (5), 914.

[62] Altaf, F., Gill, R., Batool, R., Drexler, M., Alamgir, F., Abbas, G., and Jacob, K., 2019, Proton conductivity and methanol permeability study of polymer electrolyte membranes with range of functionalized clay content for fuel cell application, *Eur. Polym. J.*, 110, 155–167.

[63] Shaari, N., Kamarudin, S.K., Basri, S., Shyuan, L.K., Masdar, M.S., and Nordin, D., 2018, Enhanced proton conductivity and methanol permeability reduction via sodium alginate electrolyte–sulfonated graphene oxide bio-membrane, *Nanoscale Res. Lett.*, 13 (1), 82.

[64] Wang, L., Dou, L., and Yang, Z., 2021, Electrospun and cross-linked nanofiber composite poly(aryl ether sulfone) for anion exchange membranes, *J. Polym. Res.*, 28 (8), 276.

[65] Zang, H., Li, Y., Li, Y., Chen, L., Du, Q., Zhou, K., Li, H., Wang, Y., and Ci, L., 2019, Adsorptive removal of cationic dye from aqueous solution by graphene oxide/cellulose acetate composite, *J. Nanosci. Nanotechnol.*, 19 (8), 4535–4542.

[66] Goldstein, J.I., Newbury, D.E., Michael, J.R., Ritchie, N.W., Scott, J.H.J., and Joy, D.C., 2018, *Scanning Electron Microscopy and X-Ray Microanalysis* (4th Ed.), Springer, New York, US.

[67] Bazbouz, M.B., and Russell, S.J., 2018, Cellulose acetate/sodium-activated natural bentonite clay nanofibres produced by free surface electrospinning, *J. Mater. Sci.*, 53 (15), 10891–10909.

[68] Üregen, N., Pehlivanoğlu, K., Özdemir, Y., and Devrim, Y., 2017, Development of polybenzimidazole/graphene oxide composite membranes for high temperature PEM fuel cells, *Int. J. Hydrogen Energy*, 42 (4), 2636–2647.

[69] Yuliwati, E., Ismail, A.F., Sean, G.P., and Martini, S., 2022, TiO_2-enabled polyvinylidene fluoride for palm oil mill effluent treatment: Effects of membrane morphology and aeration on flux and suspended solid removal, *J. Teknol.*, 84 (1), 107–115.

[70] Sinha Ray, S., Lee, H.K., Huyen, D.T.T., Park, Y.I., Park, H., Nam, S.E., Kim, I.C., and Kwon, Y.N., 2021, Fluorine-free anti-droplet surface modification by hexadecyltrimethoxysilane-modified silica nanoparticles-coated carbon nanofibers for self-cleaning applications, *Prog. Org. Coat.*, 153, 106165.

[71] Rasool, M.A., Van Goethem, C., and Vankelecom, I.F.J., 2020, Green preparation process using methyl lactate for cellulose-acetate-based nanofiltration membranes, *Sep. Purif. Technol.*, 232, 115903.

[72] Li, Y., Guo, Z., Li, S., and Van der Bruggen, B., 2021, Interfacially polymerized thin-film composite membranes for organic solvent nanofiltration, *Adv. Mater. Interfaces*, 8 (3), 2001671.

[73] Colpan, C.O., Nalbant, Y., and Ercelik, M., 2018, Fundamentals of fuel cell technologies, *Compr. Energy Syst.*, 4, 1107–1130.

[74] Rawal, N., Solanki, S., and Shah, D., 2020, Green synthesis of reduced graphene oxide with *in situ* decoration of metal nanoparticles for charge storage application, *Mater. Today: Proc.*, 21, 2066–2071.

[75] Simari, C., Enotiadis, A., Lo Vecchio, C., Baglio, V., Coppola, L., and Nicotera, I., 2020, Advances in hybrid composite membranes engineering for high-performance direct methanol fuel cells by alignment of 2D nanostructures and a dual-layer approach, *J. Membr. Sci.*, 599, 117858.

Accepted